Crystal structure of submicron-sized sulfur particles using 3D ED obtained in atmospheric conditions

Peer-reviewed author version

Rahimisheikh, Sepideh; Hajizadeh, Amirhossein; Quintelier, Matthias; STULENS, Sander; HARDY, An & Hadermann, Joke (2025) Crystal structure of submicron-sized sulfur particles using 3D ED obtained in atmospheric conditions. In: Acta Crystallographica Section C-structural Chemistry, 81 (2) , p. 56 -63.

DOI: 10.1107/S2053229625000130

Crystal structure of submicron-sized sulfur particles using 3D ED obtained in atmospheric conditions

Sepideh Rahimi[a], Amirhossein Hajizadeh[a], Matthias Quintelier[a], Sander Stulents[b], An Hardy[b] and Joke Hadermann[a]*

[a]Electron Microscopy for Materials Science (EMAT), University of Antwerp, Groenenborgerlaan 171, Antwerp, 2020, Belgium

[b]Institute for Materials Research (imo-imomec) and Energyville, Hasselt University, Hasselt, Belgium

Correspondence email: joke.hadermann@uantwerpen.be

Abstract: Lithium-sulfur batteries are a promising candidate for the next generation of rechargeable batteries. Despite extensive research on this system over the last decade, a complete understanding of the phase transformations has remained elusive. Conventional in-situ powder X-ray diffraction has struggled to determine the unit cell and space group of the polysulfides formed during charge and discharge cycles due to the high solubility of these solid products in the liquid electrolyte. With the improvement in *in-situ* electrochemical set-ups dedicated to transmission electron microscopes, three-dimensional electron diffraction (3D ED) has the potential to capture the crystal structures of the polysulfides during cycling. In this work, the structure solution and refinement from 3D electron diffraction data of elemental sulfur, known to sublimate in the vacuum of transmission electron microscopes, is enabled through the use of an environmental cell with a micro-electromechanical system. This work represents the first step in characterizing sulfur's transformation into lithium polysulfides using *in-situ* 3D ED.

Keywords: Sulfur; 3D ED; Environmental Control Holder

1. Introduction

Sulfur, as the cathode material in lithium-sulfur batteries (LSBs), offers one of the highest specific capacities (≈1675 mAh/g) and energy densities (2500 Wh kg^{-1}) among all known cathode materials for rechargeable batteries (Ting *et al.*, 2022). This property, along with sulfur's abundance, low cost, and non-toxicity, has made LSBs a key focus for next-generation rechargeable batteries. However, one of the challenges hindering commercialization is its short lifespan due to high-capacity fade (Yan *et al.*, 2016; Geng *et al.*, 2023). Many studies showed that the capacity loss is directly related to the transformation of the cathode material into the intermediate polysulfides toward the final product, Li_2S

(Ting *et al.*, 2022; Cañas *et al.*, 2013; Paolella *et al.*, 2016; Conder *et al.*, 2017; Feng *et al.*, 2014). These polysulfides are produced during the oxidation reaction of sulfur with lithium and some of the polysulfides are soluble in the electrolyte. The dissolved sulfur can diffuse toward the lithium anode, resulting in less remaining active material on the cathode side, which causes the capacity to fade (Cañas *et al.*, 2013). This phenomenon is called the shuttle effect (Mikhaylik & Akridge, 2004). The reaction in LSB transforms S_8 during cycling into polysulfides (S_n n=7,...,1) and different types of Li-S species (Li_2S_6, Li_2S_4, Li_2S_2, Li_2S). Like most of the Li compounds, Li_2S is sensitive to moisture and oxygen but S_8 is stable in air and is non-soluble in water (Cañas *et al.*, 2013). However, at room temperature, S_8 is sensitive to the vacuum and sublimates to the gas phase below a pressure of 10^{-7} kPa (Ferreira & Lobo, 2011).

In-situ powder X-ray diffraction (PXRD) could not determine the crystal structure of each phase occurring during the cycling of LSBs (Cañas *et al.*, 2013). To date, only the crystal structure of S_8, the most stable species in the system at ambient pressure, has been determined with X-ray and neutron diffraction (Pawley & Rinaldi, 1972; K. Templeton *et al.*, 2002; Steudel *et al.*, 1996; Gromilov *et al.*, 2016; Rettig Steven J. & Trotter James, 1987). The crystal structure of another polysulfide, Li_2S_2, is derived from theoretical calculations based on Density functional theory (DFT) (Feng *et al.*, 2014) and supported by in-situ PXRD data (Paolella *et al.*, 2016). The formation of other polysulfides was only inferred from broad peaks in the diffraction patterns, which could not be described using known structures from the Li-S system (Conder *et al.*, 2017). Determining the correct crystal structures of these polysulfides remains a challenge (Tan *et al.*, 2017). Since the crystals of intermediate phases remain too small for single-crystal X-ray diffraction (SCXRD) during cycling, 3D electron diffraction (3D ED), which can solve and refine the crystal structure of submicron-sized particles (Kolb *et al.*, 2007; Gemmi *et al.*, 2019; Kaiukov *et al.*, 2020), appears to be a more suitable technique. To our knowledge, no electron diffraction studies on sulfur have been performed so far. Obtaining transmission electron microscopy (TEM) data, such as electron diffraction, from pristine sulfur is challenging because sulfur sublimates under the ultra-high vacuum conditions of TEM (typically about 10^{-8} kPa) (Ferreira & Lobo, 2011; Nash, 1987; Ronan *et al.*, 2022; Raiß *et al.*, 2014). Some studies have demonstrated that images and elemental maps can be captured using cryo-TEM (Levin *et al.*, 2017; Sahore *et al.*, 2016). However, the polysulfides form during electrochemical reactions, which cannot be studied at cryogenic temperatures, because the liquid electrolyte used in Li-S batteries would freeze, reducing ion mobility. Therefore, cryo-TEM is not suitable for determining the structure of polysulfides.

In-situ 3D ED can be used to study the evolution of crystal structures during electrochemical reactions by employing dedicated electrochemical MEMS (micro-electromechanical systems) (Karakulina *et al.*, 2018). However, the use of these cells limits the tilt range to 40-60°, depending on the pole piece gap of the microscope, which is often insufficient for solving low symmetry structures like sulfur S_8. To increase the completeness, datasets from multiple crystals are merged. In case of possible phase

transitions or multi-phased samples, one should be careful to merge only crystals from the same phase (Huang *et al.*, 2021).

As a first step toward determining the structure of the polysulfides using *in-situ* electrochemistry 3D ED, this paper demonstrates that it is possible to solve and refine the structure of S_8 – despite its tendency to sublimate in vacuum and its sensitivity to the electron beam – by using 3D ED data collected at room temperature with an environmental MEMS cell (similar to the electrochemical cell) filled with air.

This method can also be applied to acquire quantitative electron diffraction data for structure solution and refinement of other materials that are sensitive to the high vacuum inside a TEM column, such as certain metal-organic frameworks (MOFs), organic compounds, and materials containing water. An example using the MOF UiO-68 will be presented. MOFs consist of metal nodes and organic linkers, and their synthesis involves wet chemistry, leading to pores filled with residual solvents and unbound linkers. A process known as 'activation' is used to empty the pores, involving solvent exchange, exposure to low-vacuum, heating, or a combination of these methods. Unfortunately, MOFs can experience structural collapse during activation due to external pressure or capillary stress (A. Dodson *et al.*, 2018; Aldin Mohamed *et al.*, 2022; Manning *et al.*, 2023). This collapse complicates structural studies using TEM, especially for MOFs with larger linkers (e.g., UiO-68) or high flexibility (e.g., MOF-5), making characterization more difficult. However, a full introduction to MOFs is beyond the scope of this paper and can be found by the interested reader in the works of Furukawa et al., Zhou et al., and Gropp et al. (Furukawa *et al.*, 2013; Zhou *et al.*, 2012; Gropp *et al.*, 2020)

2. Methods

To synthesize the sulfur particles, 2.37 g of anhydrous $Na_2S_2O_3$ (Acros organics) was dissolved in 50 ml water and slowly added into 500 ml of a dilute 3mM sulfuric acid aqueous solution (Sigma Aldrich 95-97%) containing 1 wt% polyvinylpyrrolidone (PVP, Mw~40,000 Sigma Aldrich). After stirring at room temperature for 2 hours at 600 rpm, the sulfur particles were collected by centrifugation (10000 rpm for 5 minutes). The particles were then washed with water 3 to 5 times and dried at 60°C overnight, yielding 70 mg of powder. For environmental scanning electron microscopy (ESEM) imaging, the powder was applied directly to cohesive carbon tape (PELCO Tabs).

For imaging in TEM and to obtain 3D ED data at room temperature, we used a closed environmental cell, specifically a DENSsolutions Nano-Reactor, and a DENSsolutions Climate holder. The sulfur powder was ground in a mortar with distilled water for 2 minutes and the resulting suspension was transferred to a glass vial and diluted with additional distilled water. The suspension was sonicated in an ultrasonic bath for 10 minutes and then allowed to rest for half an hour until the larger agglomerates had settled. 2 µl of the settled suspension was taken with a dispenser and drop-casted on a Nano-Reactor. The Nano-Reactor was then heated with an infrared lamp to evaporate the liquid. Once dry, the reactor

was assembled on the holder and transferred to the TEM. All preparations were performed in ambient air. To avoid the conventional vacuum environment of the TEM, we opened the inlet and outlet of the Nano-Reactor to allow room air into the system, creating an ambient air environment.
Images of the sulfur particles were captured using a ThermoFisher Tecnai G2 TEM and a ThermoFisher Quanta 250 ESEM. In the ESEM, a pressure control aperture was connected, and the atmosphere inside the chamber was air at 1150 Pa pressure. Further increasing the gas pressure inside the chamber decreased the signal-to-noise ratio.

For 3D ED data acquisition, a ThermoFisher Tecnai G2 operating at a voltage of 200 kV was used, with a tilt range of 60° (-30° to +30°) and a stage rotation speed of 1° per second, controlled by an in-house script. The microscope was set to nanobeam electron diffraction (NED) in TEM mode using a 20μm condenser aperture. Various gun lens and spot size combinations were tested to optimize electron beam intensity, with the results detailed in the Results section. After determining the optimal electron flux, the same acquisition parameters were used for all subsequent experiments. Crystals were manually selected, and no crystal tracking was used during rotation as the crystal position was stable at eucentric height. Data collection was performed using an ASI CheeTah Timepix3 Direct Electron Detector (DED) at a recording speed of 10 frames per second (fps), producing 600 frames per dataset over a total acquisition time of 1 minute. An in-house script was used to convert the frames into a format compatible with PETS2 software (Palatinus *et al.*, 2019) for the 3D reconstruction of the reciprocal space and the subsequent extraction of different sections from the reconstructed reciprocal space. Frame scaling was also done in PETS2. The intensities were exported as a reflection file in CIF-format for further processing in JANA2020 (Petříček *et al.*, 2023). Structure solution, kinematical, and dynamical refinements were carried out in JANA2020, and the resulting 3D structures were visualized using CrystalMaker (Palmer, 2015).

3. Results and discussion

Sulfur sublimates in the vacuum of an electron microscope at room temperature (Ferreira & Lobo, 2011; Nash, 1987; Ronan *et al.*, 2022; Raiß *et al.*, 2014; Levin *et al.*, 2017; Sahore *et al.*, 2016). To address this, we used an environmental SEM to determine the morphology and particle size of the synthesized sulfur sample (Figure 1a,b) and a closed environmental TEM cell to study the crystal structure (Figure 1c,d). The primary sulfur particles (Figure 1d) are small spheres with an average diameter of 0.55(7) μm and tend to form aggregates (Figure 1c), which can be several tens of micrometres in size (Figure 1a).

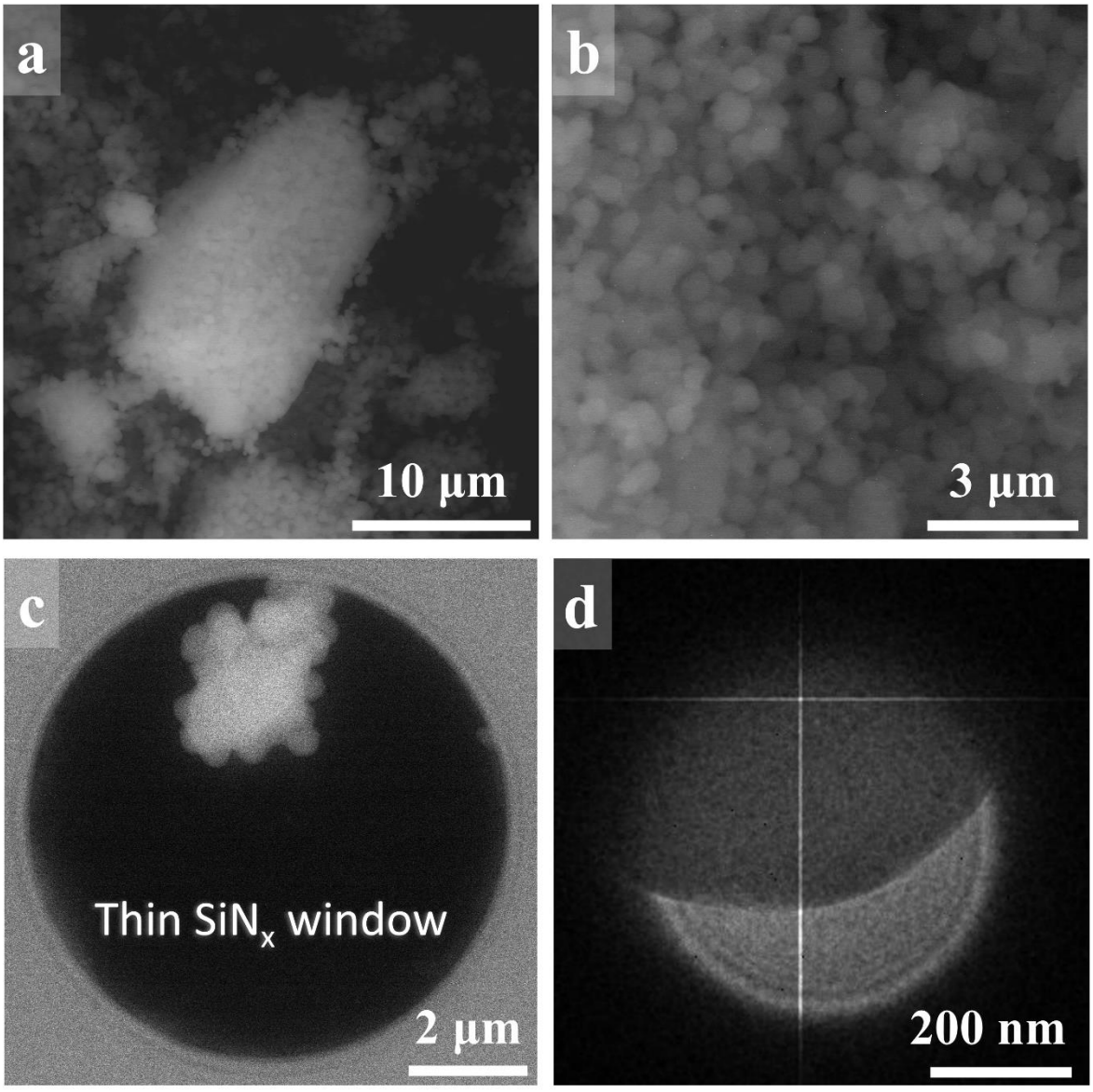

Figure 1 (a and b) ESEM, (c) STEM, and (d) TEM nanobeam images of sulfur. For the STEM image, the sample lies on the thin Si_3N_4 window of the Nano-Reactor. The TEM nanobeam image in (d) is the summation of 35 consecutive images recorded at the rate of 10 fps on the Timepix3 with 0.02 $\frac{e^-}{Å^2.s}$ electron flux.

3.1. Low-dose electron diffraction

Previous TEM studies only mentioned sulfur's sensitivity to vacuum conditions. However, when we replaced the vacuum environment with ambient air, we observed that pure elemental sulfur is also highly sensitive to the electron beam. To mitigate this effect, it was necessary to use a low-dose electron beam. To optimize the illumination conditions for achieving the best signal-to-noise ratio without damaging the sample, we monitored changes in the reflection intensities during beam exposure, using a small condenser aperture of 20µm with different combinations of gun lens and spot size (Figure 2).

Both the optimization process and the subsequent 3D ED experiments were conducted using the same electron beam size, with a diameter of 500 nm.

For the optimization, consecutive diffraction patterns were recorded from stationary particles (without any applied shift or rotation) using the ASI CheeTah DED with a 120-second exposure time. To prevent prior beam damage, each dataset was obtained from a new particle and from the random orientation in which the particle was. The reflection intensities were tracked over time at various electron fluxs (Figure 2). Detailed calculations of the electron fluxes and the diffraction patterns are provided in the Supporting Information (Figure S1). In the legends of each graph, the reflections are ordered from low to high resolution.

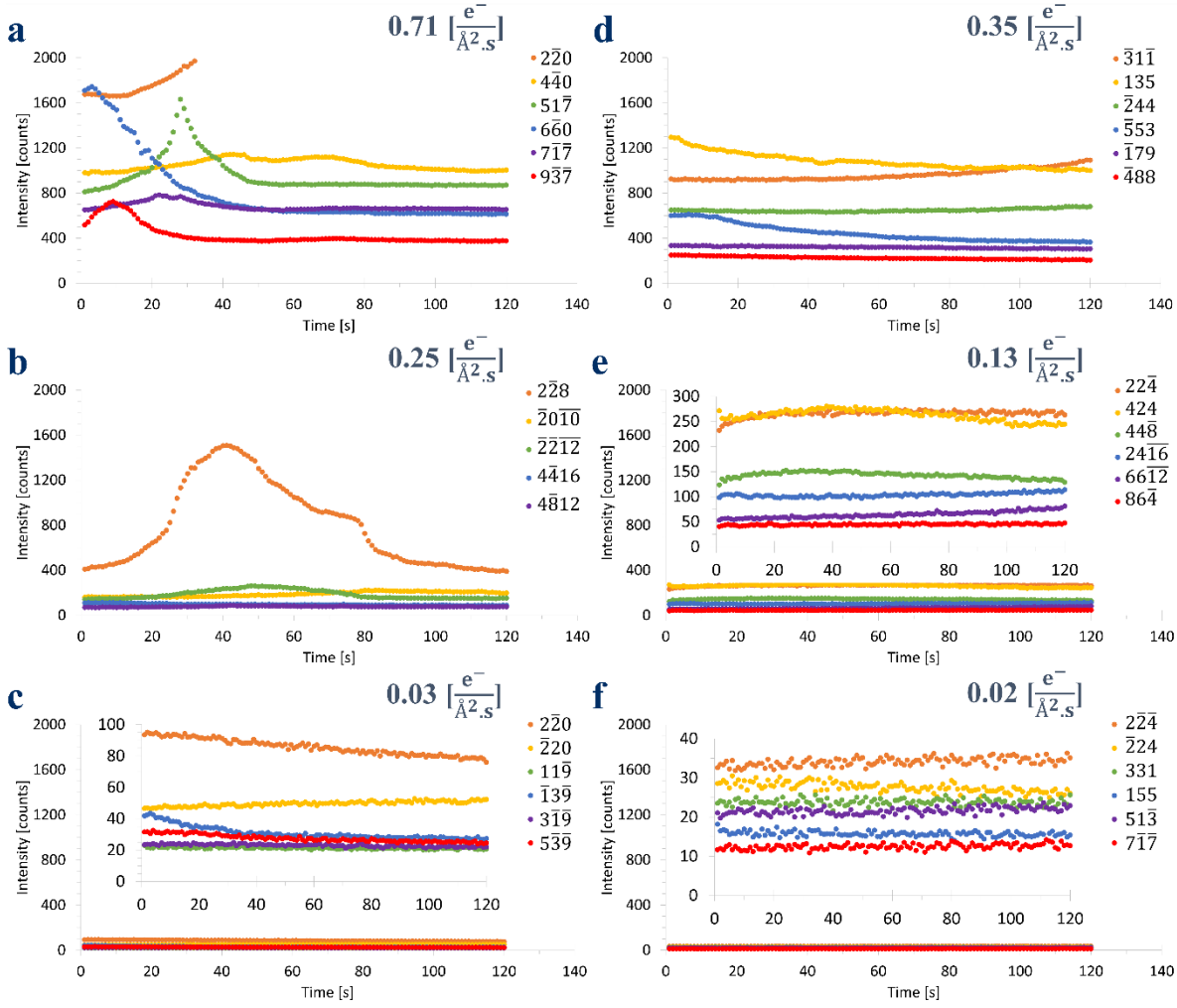

Figure 2 Intensity as a function of time for different electron fluxes, obtained by varying gun lens values and spot sizes (ThermoFisher Tecnai G2 gun lens 5 (a-c) and 8 (d-f) at spot sizes 5, 7, and 10, respectively). All graphs are shown using the same scale. The insets on c, e, and f show the region of interest at a higher scale.

Figures 2a, 2b, and 2d show that reflection intensities change significantly when using an electron flux above 0.25 $\frac{e^-}{Å^2.s}$, with, for example, a 273% change for $2\bar{2}8$ in Figure 2b. In Figures 2a and 2b, the reflection intensities do not simply decrease in intensity, as would be expected for amorphization or sublimation caused by beam damage. Instead, some reflections show an initial increase in intensity before decreasing. This could be due to structural changes (Shpanchenko *et al.*, 2001), since we observed other reflections appearing that could not be indexed with the same lattice, or to rotations of the crystals. For electron fluxes below 0.13 $\frac{e^-}{Å^2.s}$ the intensity change is lower than 20% for all reflections (Figure 2c, 2e, and 2f). At the lowest flux of 0.02 $\frac{e^-}{Å^2.s}$, no significant changes in reflection intensities are observed. The largest intensity change at this flux is 2.4(1.2) % for reflection $\bar{2}24$, and all intensity variations at this flux fall within the standard deviations, consistent with slight crystal rotations. This slow rotation is a common occurrence in TEM experiments. At even lower fluxes, hardly any reflections were found with an acceptable I/σ (intensity/standard deviation) ratio, where we used a criterion of I/σ>10 for peak identification. Therefore, all subsequent experiments in this study have been conducted using an electron flux of 0.02 $\frac{e^-}{Å^2.s}$.

3.2. Structure solution and refinement

We collected data from 10 randomly selected crystals, five of which showed single-crystal reciprocal space reconstructions, while the others contained overlapping data from multiple crystals. We proceeded with the five single-crystal data sets, labeled C1 to C5 in Table 1. The cell parameters for the reference structures from literature for S_8 obtained from single-crystal X-ray diffraction (SCXRD) studies (Cameron *et al.*, 2002; Rettig Steven J. & Trotter James, 1987) and powder X-ray diffraction (PXRD) (Sheha *et al.*, 2023) at room temperature and ambient pressure are also included in Table 1.

The cell parameters derived from the 3D ED datasets are close to those reported in the literature but vary a lot, which can be due to optical distortions, mechanical instabilities or residual radiation damage (Brázda et al., 2022). Moreover, as sulfur is an insulator, it can accumulate charge, which may influence the position of the reflections and thus the accuracy of the cell parameters (Brubaker & Fuller, 1945). The high standard deviation for C4 shows that the measurement for this crystal is less precise than that for the other crystals. This is likely due to the fact that the higher-resolution reflections are broadened in the cylindrical projection of this particle C4 (Supplementary Information Figure S9) whereas this was not the case for all other particles. This can also explain the higher R-values for this particle.

Table 1 Comparison of the different datasets. R_{int}(obs) and R_{int}(all) express the agreement and consistency of the reflections with the chosen *mmm* Laue class, with obs considering only the

observed reflections and all considering all expected reflections within the chosen resolution. d_{max} is the chosen cutoff resolution, excluding reflections at higher resolutions that deteriorated the results.

Dataset	C1	C2	C3	C4	C5*	SCXRD from ref. (Cameron *et al.*, 2002)	SCXRD from ref. (Rettig Steven J. & Trotter James, 1987)	PXRD from ref. (Sheha *et al.*, 2023)
a [Å]	10.495(8)	10.647(2)	10.371(9)	10.38(2)	10.39(1)	10.393(2)	10.4646(1)	10.47724(8)
b [Å]	12.788(9)	12.901(5)	12.892(5)	12.95(3)	13.06(2)	12.762(3)	12.8660(1)	12.88022(7)
c [Å]**	24.94(2)	24.118(5)	24.368(8)	24.48(5)	24.58(3)	24.436(5)	24.4860(3)	24.50233(7)
Volume [Å^3]	3347(4)	3312(2)	3258(3)	3290(12)	3335(7)	3241(1)	3292.74(6)	3306.57(3)
Indexed reflections [%]	92.07	99.61	97.24	100	99.05	-	-	-
d_{max} [Å]	0.93	0.96	1.09	0.94	0.96	-	-	-
No. of integrated reflections (obs/all)	146/498	59/421	65/242	90/448	50/385	-	-	-
Redundancy	2.90	2.07	3.57	2.70	2.56	-	-	-
Completeness [%]	78	74	61	75	67	-	-	-
Mosaicity (°)	0.091	0.103	0.054	0.060	0.065	-	-	-
R_{int}(obs) [%]	10.77	11.98	14.18	23.09	16.23	-	-	-
R_{int}(all) [%]	20.35	37.02	26.29	32.29	18.43	-	-	-

*tilt range 53°
** $\alpha = \beta = \gamma = 90°$

The reflection conditions were derived from dataset C6, which was not one of the completely single crystal datasets C1 - C5, as this one showed most clearly the reflection conditions. Figure 3 presents sections of the reciprocal lattice reconstructed from dataset C6. (Reciprocal sections for the datasets in Table 1 are provided in Figure S3-S7 in the Supporting Information. The single-crystal datasets showed conflicting reflection conditions, likely due to multiple diffraction effects (See Figure S8).)

The reflection conditions derived from the *h0l*, *hk0*, and *0kl* sections are *h0l*:*h*+*l*=4*n*; *h*,*l*=2*n*, *0kl*:*k*+*l*=4*n*; *k*,*l*=2*n*, and *hk0*:*h*+*k*=4*n*; *h*,*k*=2*n*. By examining additional sections, such as *h1l*, the general reflection condition *hkl*: *h*+*k*=2*n*, *k*+*l*=2*n*, *h*+*l*=2*n* can be deduced. These reflection conditions correspond to the *Fddd* space group, consistent with previous studies (Gromilov *et al.*, 2016; K. Templeton *et al.*, 2002; Rettig Steven J. & Trotter James, 1987).

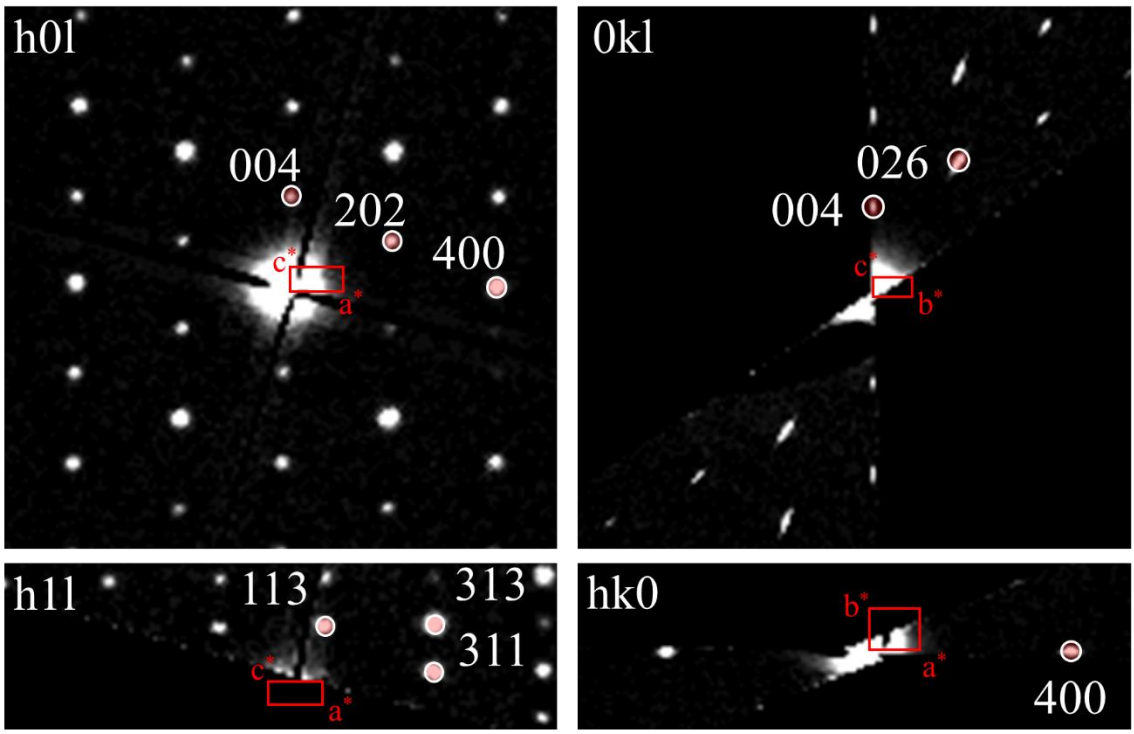

Figure 3 The indexed reciprocal sections from which the reflection conditions for the *Fddd* space group (as mentioned in the text) were derived.

For the structure solution, we used charge flipping (Superflip in Jana 2020 (Palatinus & Chapuis, 2007)). The datasets were limited in tilt range, with completeness ranging from 61% to 78%. To improve completeness, we also merged all five datasets into a single block with different scaling factors using Jana2020, following the approach outlined by Huang et al. (Huang *et al.*, 2021), further called the merged dataset. The datasets have good resolution, for example, 0.67Å for C5, however, we used higher cutoff values (Table 1) because including reflections at higher resolutions deteriorated the results.

The structure solution was performed using the kinematical file of each individual crystal, obtained from PETS2, as well as the merged dataset. Table 2 presents the space groups and R-values obtained from charge flipping for each individual dataset and for the merged dataset. All solutions produced visually similar crystal structures, although with varying space groups, suggesting minor differences between the structures. The solutions corresponded to the S_8 molecule previously reported in the literature. However, only the solution from the merged dataset had the correct space group, *Fddd* (Rettig Steven J. & Trotter James, 1987), and also showed a significantly lower R-value. Therefore, this model was used as an input model for further refinement.

Table 2 Proposed space groups from the solution for each dataset. To facilitate comparison, C5 is retained in the same unit cell as the other crystals, with the unconventional space group *F1*, instead of reducing it to the conventional *P1*.

Dataset	C1	C2	C3	C4	C5	Merged
Space group	*Fdd2*	*Fd2d*	*Fd2d*	*Fd2d*	*F1*	*Fddd*
R-value	40.84	46.97	60.20	50.47	54.10	25.62

The structure model was first refined using the kinematical approximation with isotropic atomic displacement parameters (ADPs). The kinematical refinement assumes a single scattering of the electrons by the crystal. The cutoff resolution for the merged data was set to the highest one among the individual datasets, which was 0.93Å. When anisotropic ADPs were applied, the R factors improved slightly but the refined ADPs for one atom showed a physically unacceptable small value (S4: U_{22}=0.007(4) Å^2). This issue was corrected by applying the extinction correction, an established, empirical correction used in X-ray diffraction to account for secondary extinction, i.e. when the intensity of strong reflections is reduced due to multiple scattering (Becker & Coppens, 1974; Sheldrick, 2008; Petrícek *et al.*, 2014). This correction has already been shown to improve the results for 3D ED data by compensating for multiple scattering effects (Cichocka *et al.*, 2018; Yang *et al.*, 2022; Klar *et al.*, 2023; Gholam & Hadermann, 2024). We used extinction correction as implemented in Jana2020 using the SHELX model with the value of 0.1 for all data blocks. Figure 4 visually compares the R-values resulting from the successive refinements, and the exact values are provided in the Supplementary Information, Table S2.

To account for multiple scattering, we performed the dynamical refinement using the Dyngo package within JANA2020 (Corrêa *et al.*, 2015; Palatinus *et al.*, 2013; Klar *et al.*, 2023). First, we optimized the thickness of each crystal and then refined the models obtained after kinematical refinement with isotropic ADPs. Refinement using isotropic ADPs already resulted in lower R-values compared to the kinematical approximation. The R-values improved further when refining anisotropic ADPs. After refinement, the anisotropic ADPs showed values similar to those obtained in literature in refinements against SCXRD data (Rettig Steven J. & Trotter James, 1987).

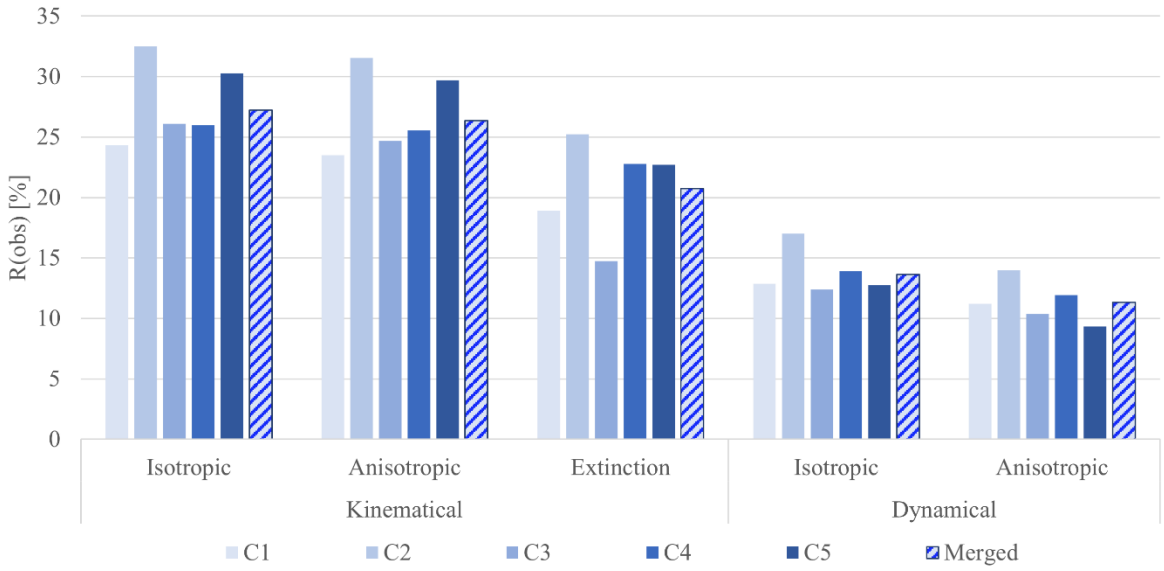

Figure 4 R-values obtained at different refinement stages

The dynamically refined structure (Figure 5) agrees better than the kinematically refined one in bond lengths and angles with the structural model from SCXRD (collection code 63082 from the ICSD database) (Rettig Steven J. & Trotter James, 1987) and PXRD (collection code 64411 from the ICSD database) (Sheha *et al.*, 2023). The maximum difference in bond lengths for the kinematically refined model with the SCXRD and PXRD model is 2.6% and 6.9% and in bond angles is 1.4% and 8.3%, respectively, while, for the dynamically refined model, compared to SCXRD and PXRD, the bond length difference is 1.4% and 4.8% and the bond angles difference is 1.1% and 7.61%, respectively. The CIF file for this dynamically refined model from the merged 5 datasets is accessible from the Supplementary Information.

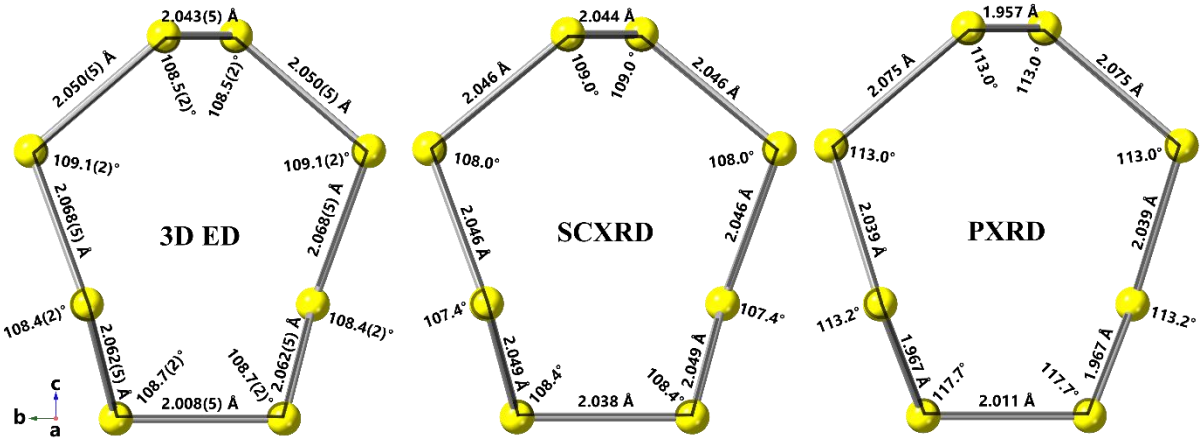

Figure 5 The projection along the *a*-axis of the model for the S_8 molecule obtained from (left) 3D ED in this work, (middle) SCXRD (Rettig Steven J. & Trotter James, 1987), and (right) PXRD (Sheha *et al.*, 2023).

These results demonstrate that the crystal structure of vacuum- and beam-sensitive materials, such as sulfur, can be accurately determined using low-dose 3D ED in a closed environmental cell, and provided data sets can be merged to overcome the limited tilt range of the cell. Based on this successful structure determination, we are confident that the crystal structures of the different polysulfides can also be determined during the electrochemical reactions using in-situ 3D ED in an electrochemical cell, despite the limited tilt and the low dose required due to the interaction between the electrolyte and the electron beam.

3.3. Extension to other materials

To demonstrate the broader applicability of the environmental cell for studying the crystal structure of other vacuum- and beam-sensitive materials besides the LSB system, we present an example involving the metal-organic framework (MOF) UiO-68.

Some MOFs, like UiO-68, collapse immediately when exposed to the ultra-high vacuum (UHV) conditions of the microscope. Typically, this issue is mitigated by plunge-freezing and using cryogenic conditions, which freeze the pore contents and prevent collapse during microscopy. However, cryogenic conditions introduce complications, such as ice formation, and, more importantly, they do not allow room temperature observations or in-situ experiments, such as activation or gas molecule incorporation. The environmental cell allows for studying native MOF structures under atmospheric conditions, similar to those in which MOFs are synthesized and used in applications, avoiding collapse caused by UHV and retaining unbound linkers and residual solvents in the pores.

As a proof-of-concept, we conducted a study on the vacuum-sensitive MOF UiO-68 ($Fm\bar{3}m$, a = 32.60Å) under atmospheric conditions. The same particle was examined in both ambient air within the environmental cell and after opening the cell to the UHV of the microscope. Figure 7 shows the particle and its corresponding diffraction patterns under atmospheric (Figure 7b) and UHV (Figure 7c) conditions. Under atmospheric conditions, the particle exhibited a clear diffraction pattern, demonstrating its crystallinity. Additionally, a one-minute exposure to the electron beam (similar to what was used for the 3D ED data acquisition of sulfur) showed no changes in the diffraction pattern (Figure 6b), ruling out beam-induced structural damage. However, upon exposure to the UHV after opening the chip, no reflections were observed any longer, indicating a vacuum-induced structural collapse. This result demonstrates the effectiveness of closed cells in preventing vacuum-induced collapse during microscopy.

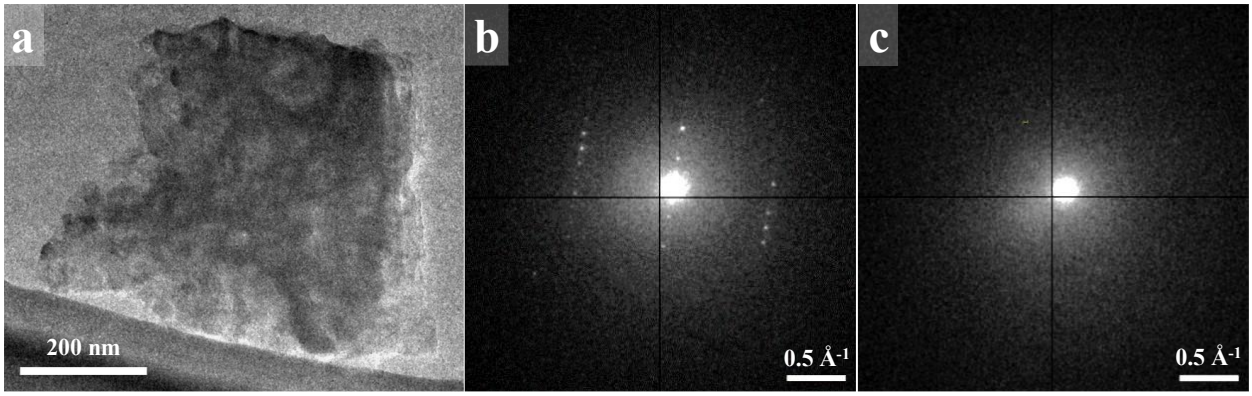

Figure 6 (a) real space image of the studied UiO-68 particle, (b and c) diffraction patterns after 60 seconds of exposure of the same particle taken at atmospheric (b) and UHV conditions (c).

Overall, there are several advantages and disadvantages when deciding between using an environmental gas cell or a cryo transfer holder. Closed environmental cells integrated into MEMS are costly, can accommodate particles only up to a certain size (typically 5 µm), and have a limited tilt range. However, they protect the particles from vacuum exposure and allow measurements at room temperature and higher. In contrast, using a cryo transfer holder to cool the sample to mitigate vacuum damage can be done with conventional, low-cost grids on particles of any size suitable for normal TEM experiments. This method also allows particles to be tilted over a wider range of angles, but cooling can alter the structure, and of course, it does not permit observations at room temperature or higher.

Sublimation can also be prevented using a graphene cell with liquid-filled pockets (Plana-Ruiz *et al.*, 2023), provided the liquid does not interact with the material. However, the primary advantage of environmental cells is the possibility to add inlets, outlets, and electrodes, enabling changes in the gas or liquid environment and biasing during in-situ experiments. This is not yet possible with graphene cells. This paper has demonstrated the possibility of obtaining accurate crystal structures from vacuum- and beam-sensitive materials using 3D ED with a closed environmental cell within a MEMS chip, paving the way for in situ 3D ED experiments on such challenging samples.

4. Conclusion

This study demonstrated the feasibility of solving and refining the structure of vacuum- and electron beam-sensitive compounds, such as the pristine S_8 phase, using an environmental cell, despite the limited tilt range imposed by the MEMS chip. The dynamically refined bond distances and angles showed good agreement with single crystal XRD results available in the ICSD database. As a proof of concept, we also successfully demonstrated that the use of the Nano-reactor mitigated vacuum-induced degradation of MOF UiO-68. The gas cell used in this study has the same configuration as an electrochemical cell, minus the electrodes and the electrolyte. For in situ 3D ED of polysulfides formed during electrochemical reactions, incorporating the electrolyte will be the next challenge for future research.

Acknowledgements The authors acknowledge the support by SIM (Strategic Initiative Materials in Flanders) and VLAIO (Flemish government agency Flanders Innovation and Entrepreneurship) within the SBO project FuGels (Grant HBC.2021.0016) in the SIM research program SIMBA –Sustainable and Innovative Materials for Batteries. Further financial support is acknowledged from the Hercules fund through FWO I003218N and the University of Antwerp through BOF TOP 38689. This project has also received funding from the European Union's Horizon 2020 research and innovation program under the Marie-Sklodowska-Curie grant agreement No 956099. The authors are grateful to Saleh Gholam for the in-house scripting of the microscope for continuous rotation data acquisition and pre-process data handling.

References

A. Dodson, R., G. Wong-Foy, A. & J. Matzger, A. (2018). *Chemistry of Materials* **30**, 6559–6565.

Aldin Mohamed, S., Kim, Y., Lee, J., Choe, W. & Kim, J. (2022). *Inorg Chem* **61**, 9702–9709.

Becker, P. J. & Coppens, P. (1974). Extinction within the Limit of Validity of the Darwin Transfer Equations. I. General Formalisms for Primary and Secondary Extinction and Their Application to Spherical Crystals.

Brázda, P., Klementová, M., Krysiak, Y. & Palatinus, L. (2022). *IUCrJ* **9**, 735–755.

Brubaker, D. G. & Fuller, M. L. (1945). *J Appl Phys* **16**, 128–130.

Cameron, T. S., Decken, A., Dionne, I., Fang, M., Krossing, I. & Passmore, J. (2002). *Chemistry - A European Journal* **8**, 3386–3401.

Cañas, N. A., Wolf, S., Wagner, N. & Friedrich, K. A. (2013). *J Power Sources* **226**, 313–319.

Cichocka, M. O., Ångström, J., Wang, B., Zou, X. & Smeets, S. (2018). *J Appl Crystallogr* **51**, 1652–1661.

Conder, J., Bouchet, R., Trabesinger, S., Marino, C., Gubler, L. & Villevieille, C. (2017). *Nat Energy* **2**, https://doi.org/10.1038/nenergy.2017.69.

Corrêa, C. A., Klementová, M. & Palatinus, L. (2015). Vol. *128*, *Acta Physica Polonica A*. pp. 651–653. Polish Academy of Sciences.

Feng, Z., Kim, C., Vijh, A., Armand, M., Bevan, K. H. & Zaghib, K. (2014). *J Power Sources* **272**, 518–521.

Ferreira, A. G. M. & Lobo, L. Q. (2011). *Journal of Chemical Thermodynamics* **43**, 95–104.

Furukawa, H., Cordova, K. E., O'Keeffe, M. & Yaghi, O. M. (2013). *Science (1979)* **341**, https://doi.org/10.1126/science.1230444.

Gemmi, M., Mugnaioli, E., E. Gorelik, T., Kolb, U., Palatinus, L., Boullay, P., Hovmöller, S. & Pieter Abrahams, J. (2019). *ACS Cent Sci* **5**, 1315–1329.

Geng, C., Qu, W., Han, Z., Wang, L., Lv, W. & Yang, Q. H. (2023). *Adv Energy Mater* **13**, https://doi.org/10.1002/aenm.202204246.

Gholam, S. & Hadermann, J. (2024). *Ultramicroscopy* **266**, https://doi.org/10.1016/j.ultramic.2024.114022.

Gromilov, S. A., Piryazev, D. A., Egorov, N. B. & Akimov, D. V. (2016). *Journal of Structural Chemistry* **57**, 1663–1666.

Gropp, C., Canossa, S., Wuttke, S., Gándara, F., Li, Q., Gagliardi, L. & Yaghi, O. M. (2020). *ACS Cent Sci* **6**, 1255–1273.

Huang, Z., Willhammar, T. & Zou, X. (2021). *Chem Sci* **12**, 1206–1219.

Jannis, D., Hofer, C., Gao, C., Xie, X., Béché, A., Pennycook, T. J. & Verbeeck, J. (2022). *Ultramicroscopy* **233**, 113423.

K. Templeton, L., H. Templeton, D. & Zalkin, Allan. (2002). *Inorg Chem* **15**, 1999–2001.

Kaiukov, R., Almeida, G., Marras, S., Dang, Z., Baranov, D., Petralanda, U., Infante, I., Mugnaioli, E., Griesi, A., De Trizio, L., Gemmi, M. & Manna, L. (2020). *Inorg Chem* **59**, 548–554.

Karakulina, O. M., Demortière, A., Dachraoui, W., Abakumov, A. M. & Hadermann, J. (2018). In situ electron diffraction tomography using a liquid-electrochemical TEM cell for crystal structure determination of cathode materials for Li-ion batteries.

Klar, P. B., Krysiak, Y., Xu, H., Steciuk, G., Cho, J., Zou, X. & Palatinus, L. (2023). *Nat Chem* **15**, 848–855.

Kolb, U., Gorelik, T., Kübel, C., Otten, M. T. & Hubert, D. (2007). *Ultramicroscopy* **107**, 507–513.

Levin, B. D. A., Zachman, M. J., Werner, J. G., Sahore, R., Nguyen, K. X., Han, Y., Xie, B., Ma, L., Archer, L. A., Giannelis, E. P., Wiesner, U., Kourkoutis, L. F. & Muller, D. A. (2017). *Microscopy and Microanalysis* **23**, 153–162.

Manning, J. R. H., Donval, G., Tolladay, M., Underwood, T. L., Parker, S. C. & Düren, T. (2023). *J Mater Chem A Mater* **11**, 25929–25937.

Mikhaylik, Y. V. & Akridge, J. R. (2004). *J Electrochem Soc* **151**, A1969.

Nash, D. B. (1987). *Icarus* **72**, 1–34.

Palatinus, L., Brázda, P., Jelínek, M., Hrdá, J., Steciuk, G. & Klementová, M. (2019). *Acta Crystallogr B Struct Sci Cryst Eng Mater* **75**, 512–522.

Palatinus, L. & Chapuis, G. (2007). *J Appl Crystallogr* **40**, 786–790.

Palatinus, L., Jacob, D., Cuvillier, P., Klementová, M., Sinkler, W. & Marks, L. D. (2013). *Acta Crystallogr A* **69**, 171–188.

Palmer, D. C. (2015). *Z Kristallogr Cryst Mater* **230**, 559–572.

Paolella, A., Zhu, W., Marceau, H., Kim, C. su, Feng, Z., Liu, D., Gagnon, C., Trottier, J., Abdelbast, G., Hovington, P., Vijh, A., Demopoulos, G. P., Armand, M. & Zaghib, K. (2016). *J Power Sources* **325**, 641–645.

Pawley, G. S. & Rinaldi, R. P. (1972). Constrained Refinement of Orthorhombic Sulphur Prentice Hall. WILLIAMS, D. E.

Petrícek, V., Dušek, M. & Palatinus, L. (2014). *Zeitschrift Fur Kristallographie* **229**, 345–352.

Petříček, V., Palatinus, L., Plášil, J. & Dušek, M. (2023). *Z Kristallogr Cryst Mater* **238**, 271–282.

Plana-Ruiz, S., Gómez-Pérez, A., Budayova-Spano, M., Foley, D. L., Portillo-Serra, J., Rauch, E., Grivas, E., Housset, D., Das, P. P., Taheri, M. L., Nicolopoulos, S. & Ling, W. L. (2023). *ACS Nano* **17**, 24802–24813.

Raiß, C., Peppler, K., Janek, J. & Adelhelm, P. (2014). *Carbon N Y* **79**, 245–255.

Rettig Steven J. & Trotter James (1987). Refinement of the structure of orthorhombic sulfur Kynoch Press.

Ronan, O., Downing, C. & Nicolosi, V. (2022). *Open Research Europe* **2**, 1.

Sahore, R., Levin, B. D. A., Pan, M., Muller, D. A., DiSalvo, F. J. & Giannelis, E. P. (2016). *Adv Energy Mater* **6**, https://doi.org/10.1002/aenm.201600134.

van Schayck, J. P., van Genderen, E., Maddox, E., Roussel, L., Boulanger, H., Fröjdh, E., Abrahams, J. P., Peters, P. J. & Ravelli, R. B. G. (2020). *Ultramicroscopy* **218**, 113091.

Sheha, E. M., Farrag, M., Refai, H. S., El-Desoky, M. M. & Abdel-Hady, E. (2023). *Physica Status Solidi (A) Applications and Materials Science* **220**, https://doi.org/10.1002/pssa.202200661.

Sheldrick, G. M. (2008). *Acta Crystallogr A* **64**, 112–122.

Shpanchenko, R. V., Chernaya, V. V., Abakumov, A. M., Antipov, E. V., Hadermann, J., Van Tendeloo, G., Kaul, E. E., Geibel, C., Sheptyakov, D. & Balagurov, A. M. (2001). *Z Anorg Allg Chem* **627**, 2143–2150.

Steudel, R., Bergemann, K., Buschmann, J. & Luger, P. (1996). *Inorg Chem* **35**, 2184–2188.

Tan, J., Liu, D., Xu, X. & Mai, L. (2017). *Nanoscale* **9**, 19001–19016.

Ting, L. K. J., Gao, Y., Wang, H., Wang, T., Sun, J. & Wang, J. (2022). *ACS Omega* **7**, 40682–40700.

Yan, J., Liu, X. & Li, B. (2016). *Advanced Science* **3**, https://doi.org/10.1002/advs.201600101.

Yang, T., Xu, H., Zou, X. & Borbély, A. (2022). *J Appl Crystallogr* **55**, 1583–1591.

Zhou, H. C., Long, J. R. & Yaghi, O. M. (2012). *Chem Rev* **112**, 673–674.

Supporting information

S1. Electron flux measurement and optimization

During each measurement, the size of the condenser aperture (20 μm) and the strength of the condenser lens were kept constant. The signal was recorded on a direct electron detector (ASI Timepix3). To calculate the flux, the averaged intensity (in counts) over a few pixels was measured from a flat picture of the beam integrated over 1 second of exposure. Subsequently, the value was divided by the size of the pixel (in $Å^2$) scaled by the magnification and the calculated PSF (Point Spread Function) value. We calculated the PSF for this detector 4.4 pixels at 200kV accelerating voltage with a Digital-to-Analogue Converter (DAC) setting equal to 6 (arbitrary units) based on the methods indicated in the literature (Figure S1) (Jannis *et al.*, 2022; van Schayck *et al.*, 2020).

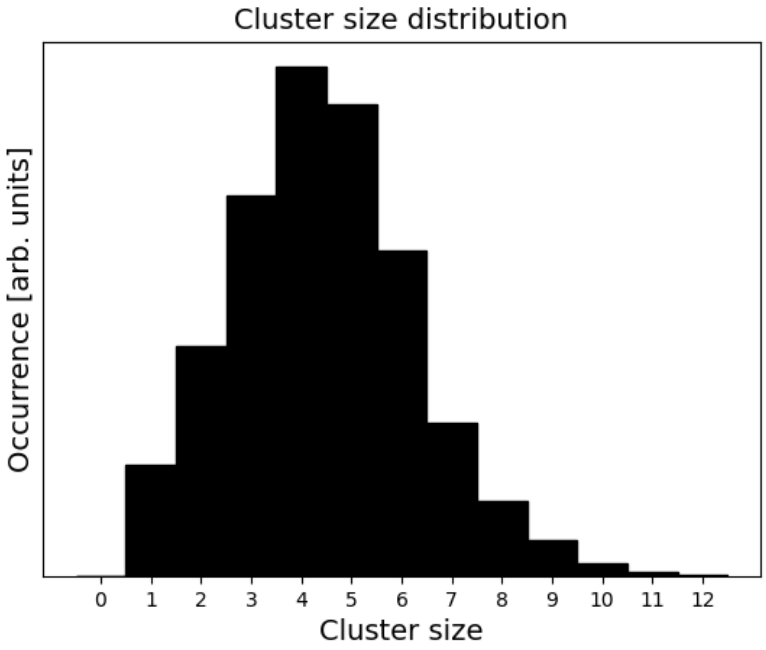

Figure S1 Histogram showing the cluster size distribution for 1 incoming electron at an accelerating voltage of 200kV and a DAC setting equal to 6 (arbitrary units).

Calculated electron flux for different illumination conditions.The following table shows the calculated values for the flux.

Table S1 Calculated electron flux for different illumination conditions.

Gun lens	5			6			8			
Spot size	5	7	10	5	7	10	5	7	9	10
Mean intensity	1.9(2)*	0.66(5)	0.077(9)	1.36(7)	0.52(5)	0.060(9)	0.90(6)	0.33(3)	0.08(1)	0.045(7)

[in 10^3 counts]										
Electron flux [$\frac{e^-}{Å^2.s}$]	0.71(6)	0.25 (2)	0.029(3)	0.52(3)	0.20(2)	0.023 (3)	0.36(2)	0.13(1)	0.032(4)	0.017 (3)

*numbers in the parentheses are the standard deviation

Diffraction patterns were recorded from different particles exposed to the indicated electron fluxes above. Figure S2 shows the diffraction patterns for the 6 electron fluxes. At each pattern, we measured the average intensity over a 32 by 32 area of pixels for every reflection separately. Then the same measurement was done over 120 frames to plot the intensity change. It should be noted that the reflections did not leave the measuring area of pixels over 120 frames.

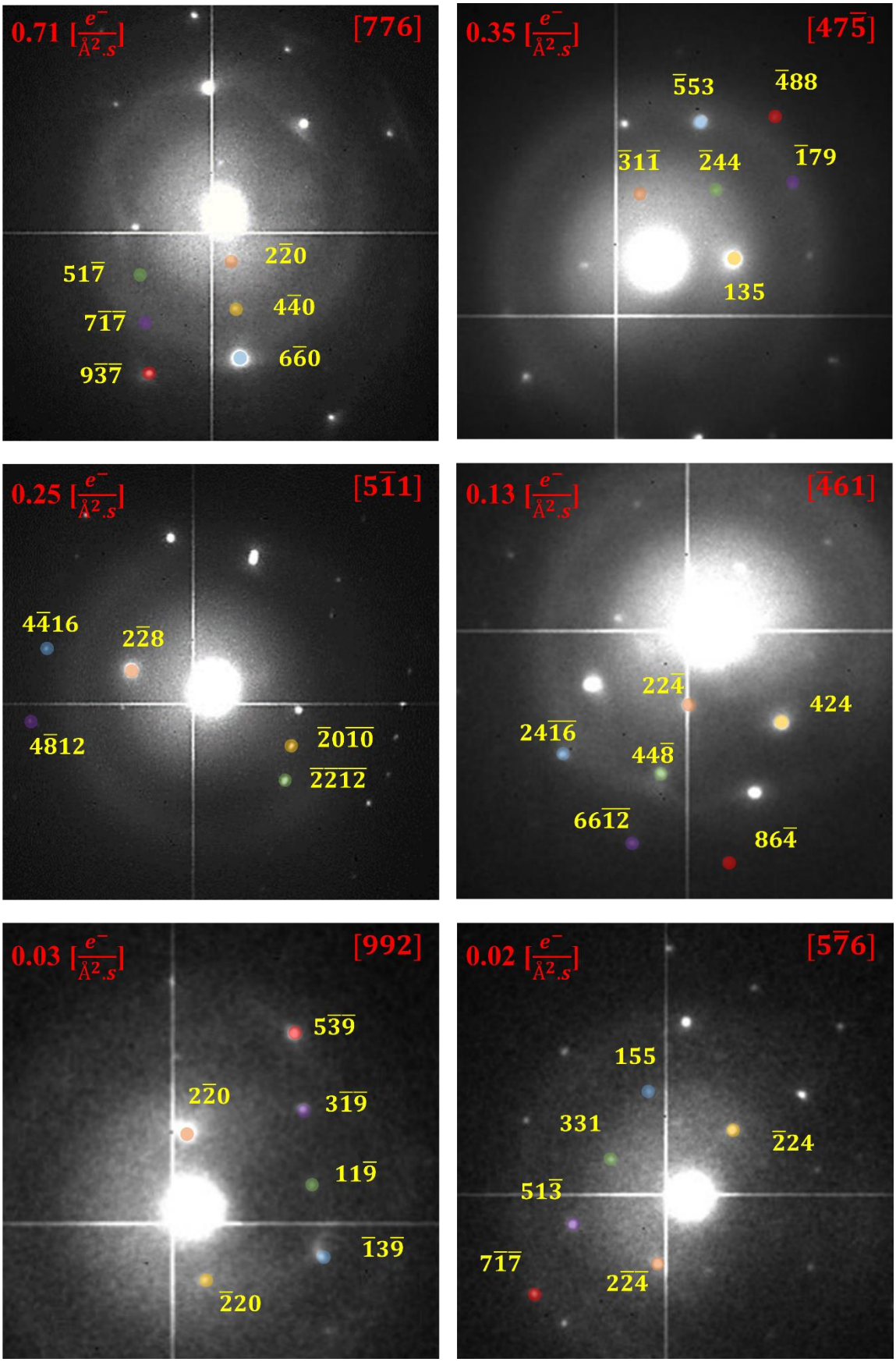

Figure S2 Diffraction patterns acquired in different electron fluxes

S2. Reciprocal sections and multiple scattering

Figures S3 to S7 show the same sections as shown before (Figure 3 in the main text) for all the datasets mentioned in Table 1 used for further data processing. Reflections not in agreement with the reflection conditions mentioned above are due to double diffraction, as shown in detail in Figure S8.

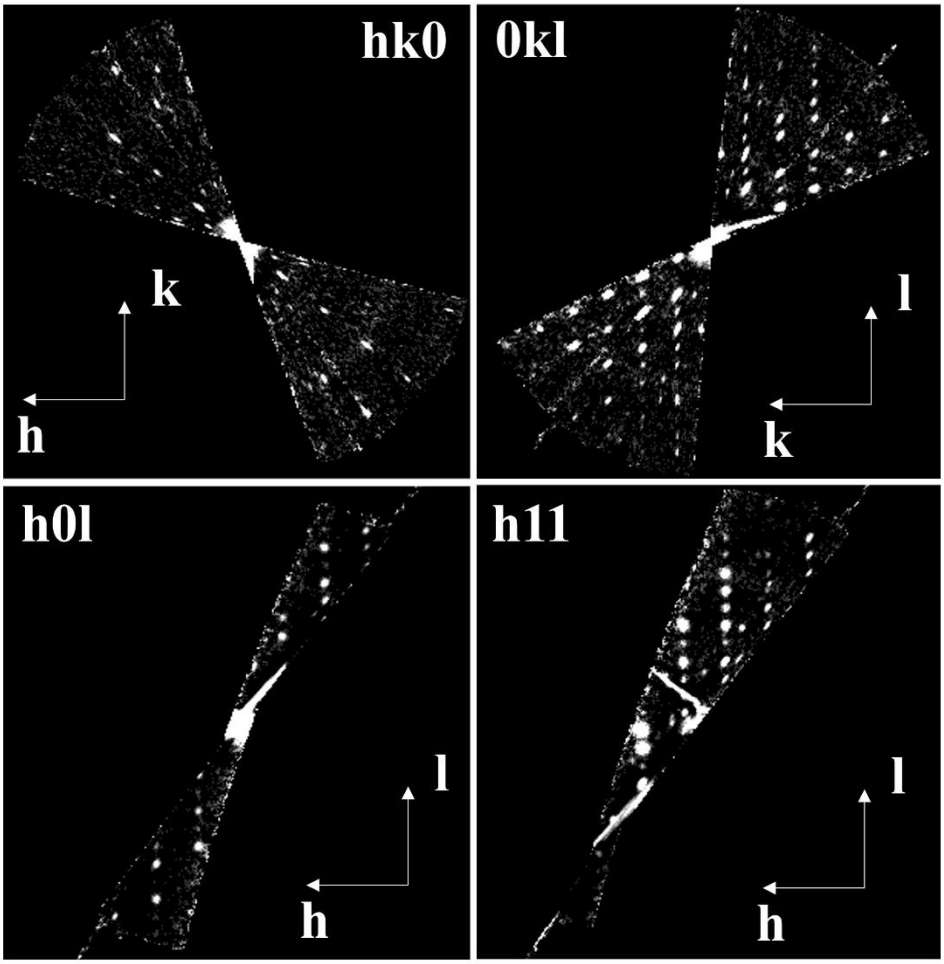

Figure S3 The reciprocal sections from 3D ED on C1

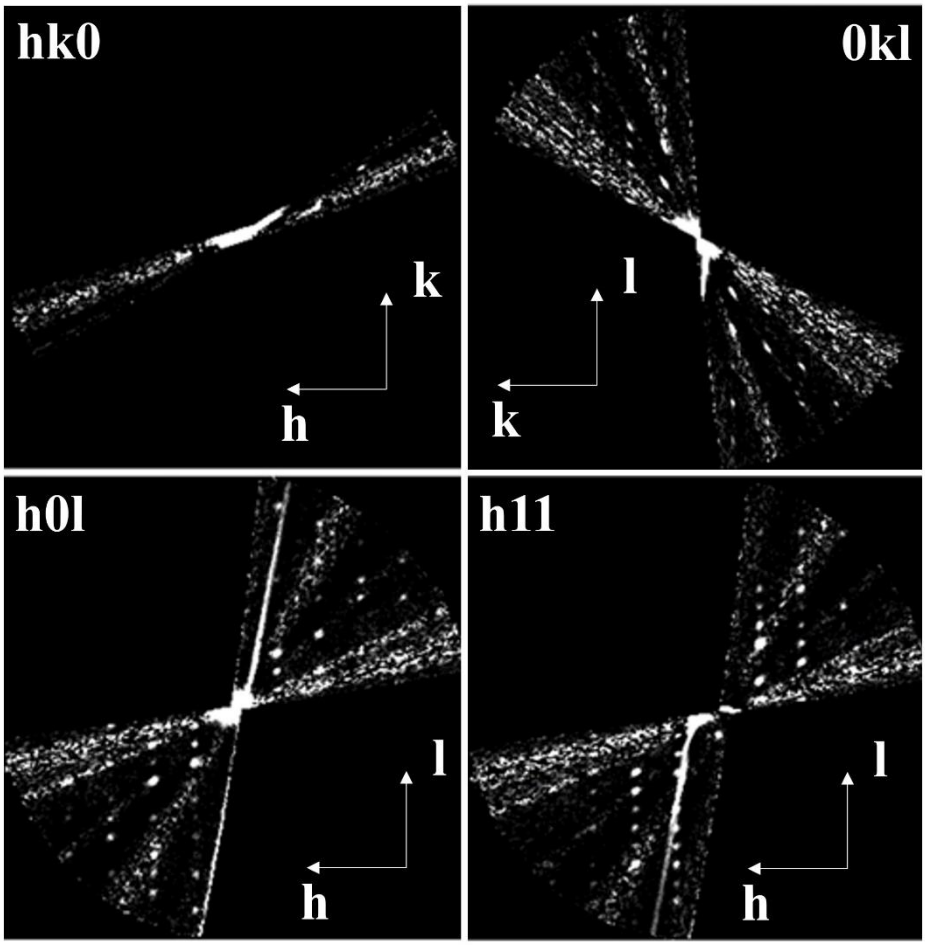

Figure S4 The reciprocal sections from 3D ED on C2

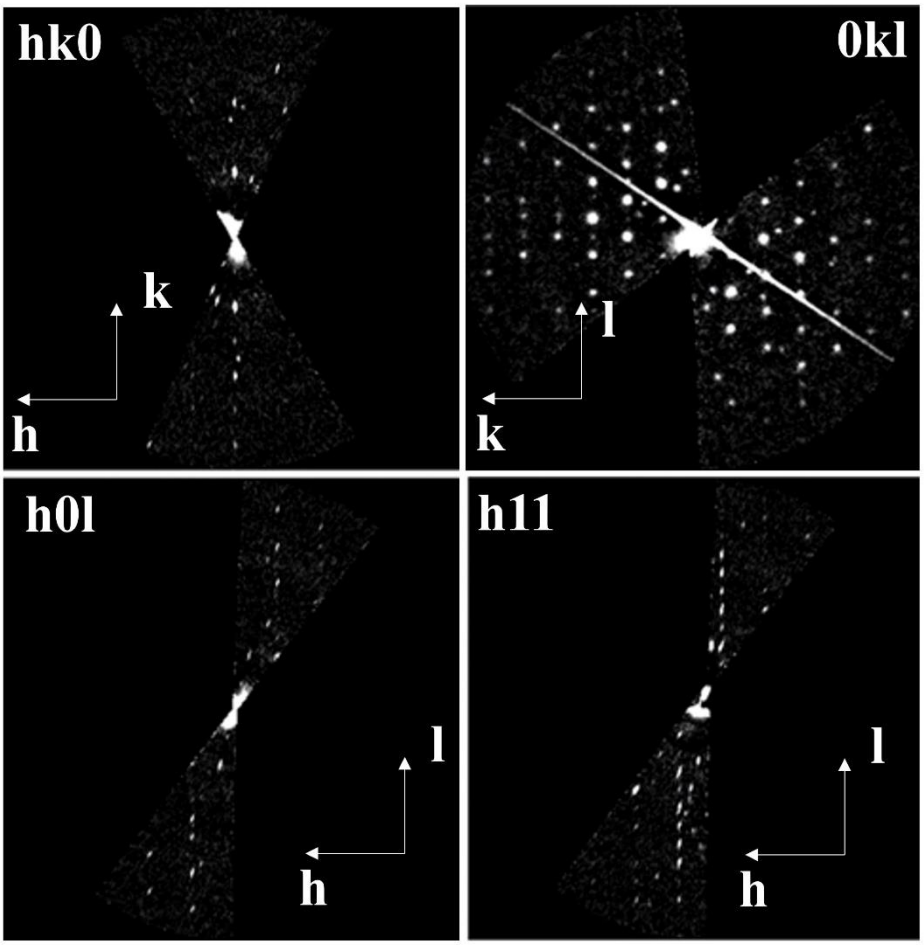

Figure S5 The reciprocal sections from 3D ED on C3

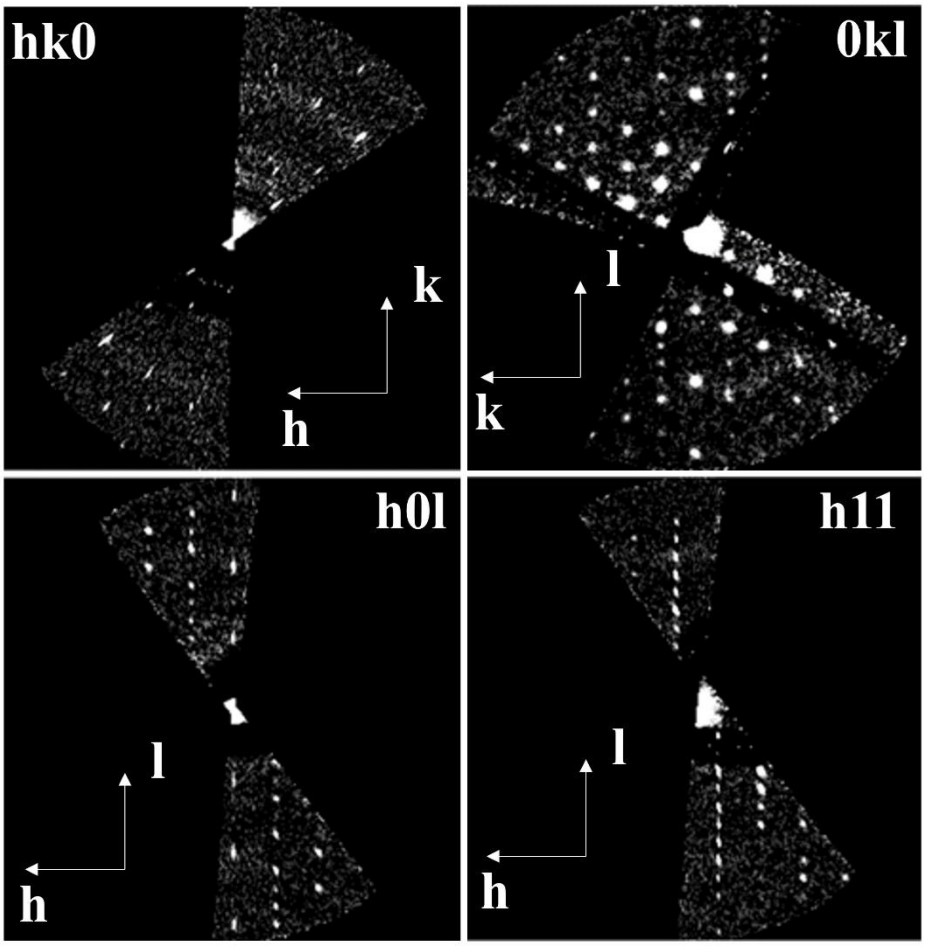

Figure S6 The reciprocal sections from 3D ED on C4

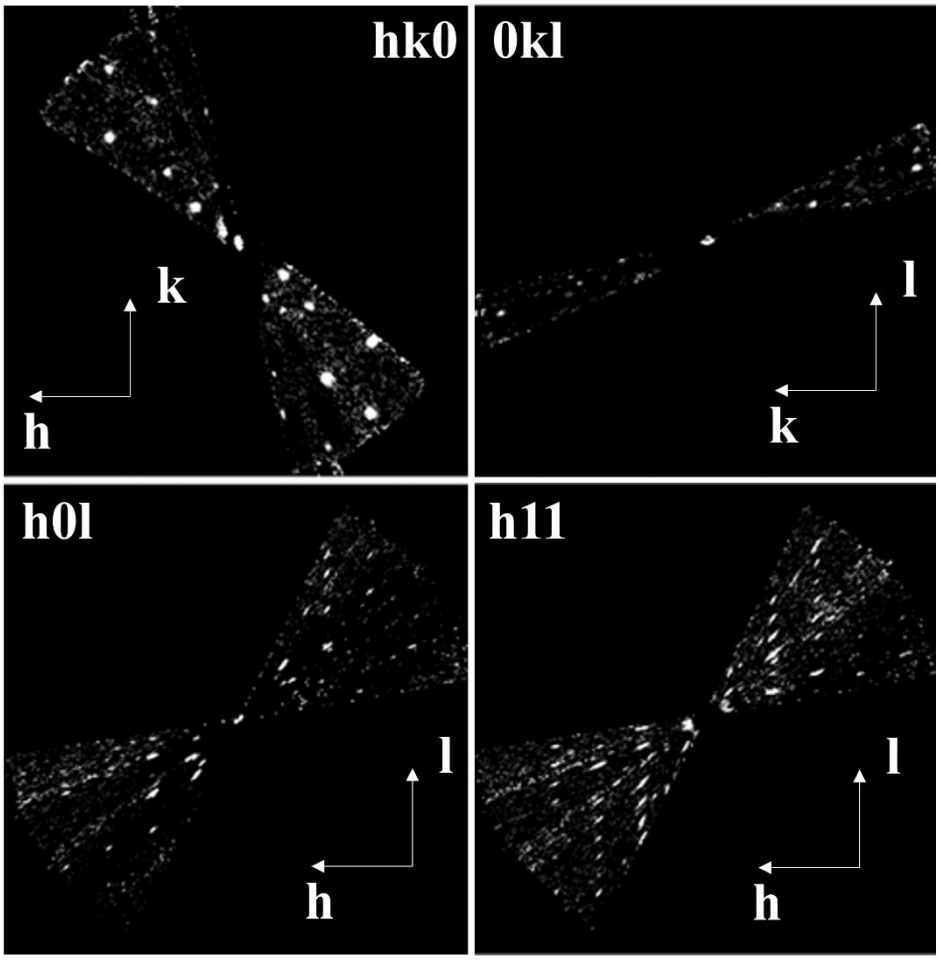

Figure S7 The reciprocal sections from 3D ED on C5

We observed reflections with low intensity (still higher than 3σ) on the generated reciprocal sections violated the reflection conditions for the *Fddd* space group (see Figure S8). In the 0kl section of the dataset C1 the $0\bar{2}\bar{8}$ violates the *k+l=4n* condition for the glide plane perpendicular to the a-axis. However, when inspecting the frame containing the $0\bar{2}\bar{8}$ reflection, the combined presence of the $3\bar{3}\bar{1}$ and $\bar{3}1\bar{7}$ reflections allow us to explain the occurrence of the $0\bar{2}\bar{8}$ reflection through double diffraction. Similar inspections were performed for the other reflections that break the *Fddd* reflections conditions and allowed assigning all those reflections to double diffraction paths.

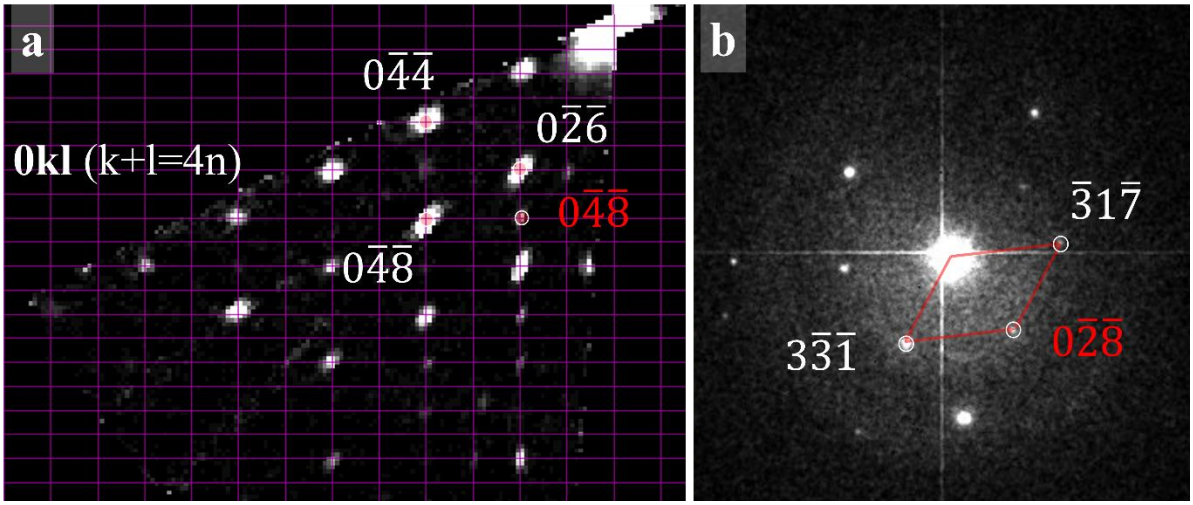

Figure S8 (a) 0kl section of dataset C1 and (b) the corresponding frame from dataset C1 that the violating reflection appears on

S3. Structure solution and refinement results

Table S2 shows the R-values obtained at the end of the refinement for each individual dataset and for the merged dataset. In the table, Iso, AIso, and Ext refer to the isotropic and anisotropic atomic displacement parameters (ADPs) and extinction correction, respectively. Also, Nr and Np indicate the number of all reflections and the number of refinement parameters, respectively. Since the kinematical refinement does not consider multiple scattering variations due to thickness change during crystal rotation, the number of refinement parameters for different crystals is the same.

Table S2 R-values [%] obtained at the end of the refinement for each individual dataset and for the merged dataset.

Dataset	ADP	Kinematical refinement						Dynamical refinement					
		Nr	Np	R(obs)	wR(obs)	R(all)	wR(all)	Nr	Np	R(obs)	wR(obs)	R(all)	wR(all)
C1	Iso	462	17	24.33	30.62	27.10	32.54	705	45	12.85	14.62	14.20	14.69
	AIso		37	23.49	30.15	26.51	32.15		65	11.21	12.42	12.43	12.49
	Ext		38	18.91	26.17	22.49	29.01						
C2	Iso	378	17	32.51	37.82	38.77	39.96	438	38	17.01	17.89	18.23	17.97
	AIso		37	31.55	36.93	38.13	39.03		58	13.98	15.48	15.30	15.55
	Ext		38	25.23	30.51	32.30	32.37						
C3	Iso	213	17	26.09	31.40	28.76	32.81	424	46	12.39	14.09	13.97	14.16
	AIso		37	24.69	29.69	27.73	31.44		66	10.46	12.41	11.85	12.47
	Ext		38	14.75	20.79	18.97	23.47						

C4	Iso	412	17	25.98	34.09	32.99	36.81	476	40	13.90	14.22	16.08	14.58
	AIso		37	25.55	33.25	32.75	35.95		60	11.87	12.84	14.27	13.31
	Ext		38	22.79	28.61	30.47	32.20						
C5	Iso	366	17	30.26	37.45	37.34	41.04	403	37	12.76	13.68	14.34	13.80
	AIso		37	29.70	36.79	35.88	39.97		57	10.20	11.67	12.07	11.84
	Ext		38	22.71	27.84	31.78	33.62						
Merged	Iso	1831	21	27.22	33.65	32.59	36.02	2446	142	13.63	14.84	15.19	14.97
	AIso		41	26.37	32.66	31.84	35.07		162	11.49	12.86	13.07	13.02
	Ext		42	20.75	26.72	27.24	29.99						

S4. Differences in the precision of the cell parameters measurement

For the C4 dataset, the higher-resolution reflections deviate from their ideal position as shown in the cylindrical projection below. This means that uncertainty of the position of the reflections in reciprocal space is high. This is also shown by the dip in the camel plot at 0.6 resolution shell, resulting in a non-ideal camel plot. Which also results in the high R values for this dataset. The reason most probably is that for this dataset the distortions caused by the TEM lenses could not be properly refined. This can explain why this measurement was the least precise among all datasets.

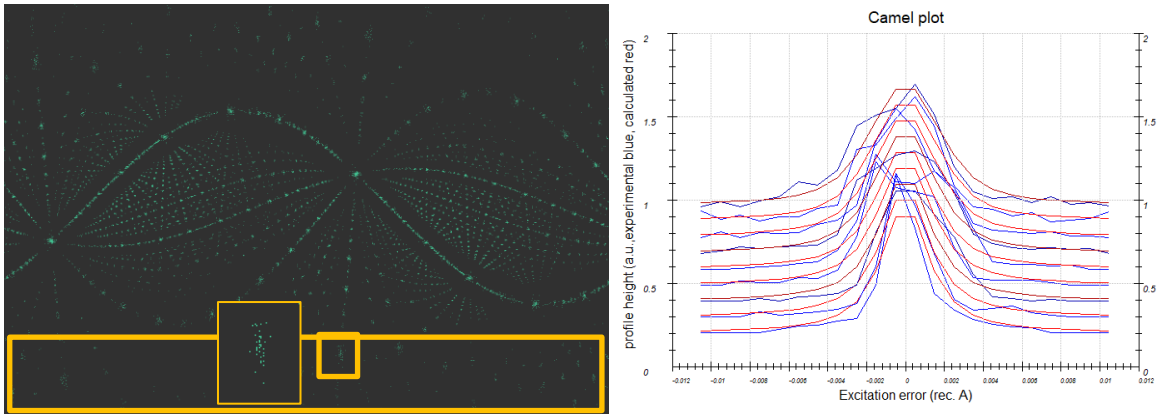

Figure S9 Cylindrical projection (left) and the Camel plot (right) of the C4 dataset